Jahn-Teller effect and large-amplitude motion in CH_4^+ studied by high-resolution photoelectron spectroscopy of CH_4

Ugo Jacovella, Hans Jakob Wörner, Frédéric Merkt *

Laboratory of Physical Chemistry, ETH Zurich, CH-8093 Zurich, Switzerland

ARTICLE INFO

ABSTRACT

This article presents the current status of the knowledge of the rovibronic energy-level structure of CH_4^+ obtained by high-resolution photoelectron spectroscopy. The results of previous investigations are summarized and extended by new results obtained by double-resonance experiments involving vacuum-ultraviolet and mid-infrared laser radiation. These experiments have led to assignments of the nuclear-spin symmetry of 303 rovibrational levels of CH_4^+ with up to $3575\ cm^{-1}$ of internal excitation. A two-dimensional model of the pseudorotational motion of CH_4^+ is also presented, with which the positions and vibronic symmetry of the low-lying vibronic levels of CH_4^+ can be predicted. The model maps the $F \otimes (f \oplus e)$ Jahn-Teller problem for the e and f_2 modes corresponding to the C—H bending motion onto a sphere, including the effects of both linear and quadratic Jahn-Teller coupling terms. The pseudorotation eigenstates are obtained by solving the two-dimensional Schrödinger equation using a basis of spherical harmonics.

© 2017 Elsevier Inc. All rights reserved.

1. Introduction

The radical cation of methane is one of the simplest molecules with a triply degenerate electronic ground state. The Jahn-Teller effect and the resulting large-amplitude nuclear motion lead to a rapid exchange of the equivalent protons and to an extraordinarily dense and complex rovibronic energy-level structure [1–5], reminiscent of the level structure of CH_5^+ [6–12] but with the additional complications arising from the degenerate nature of the electronic ground state. The elucidation of the structure and dynamics of CH_4^+ represents a very challenging problem of high-resolution molecular spectroscopy.

This article summarizes studies of the structure and dynamics of the radical cation of methane by high-resolution photoelectron spectroscopy carried out at ETH Zurich and presents new nuclear-spin-symmetry assignments of many rovibrational levels of CH_4^+ with up to $3575\ cm^{-1}$ of internal excitation and a two-dimensional model of the vibronic level structures that includes the C-H bending modes of e and f_2 symmetry.

Methane is a highly symmetric molecule and its symmetry operations have been thoroughly investigated by Hougen [13], who also summarized earlier contributions to the group-theoretical treatment of molecules of tetrahedral symmetry. CH_4 and CH_4^+ belong to the same complete-nuclear-permutation-inver-

sion (CNPI) group (G48 or S_4^*) of order 48. Symmetry assignments of the molecular orbitals and vibrational modes of methane are, however, commonly presented in the T_d point group [14] or in the $T_d(M)$ molecular-symmetry group [15], which is the subgroup of the CNPI group that arises if the inversion through the molecule center (or stereomutation [16]) is considered to be unfeasible.

The electronic configuration $(1a_1)^2(2a_1)^2(1f_2)^5$ of the $\tilde{X}^+\ ^2F_2$ electronic ground state of CH_4^+ is obtained by removing an electron from the fully occupied degenerate highest molecular orbitals $[(1f_2)^6]$ of the $\tilde{X}^1A_1$ electronic ground state of CH_4. It is therefore triply degenerate and subject to the $F \otimes (f \oplus e)$ Jahn-Teller effect (see Refs. [17–19] and references therein). The Jahn-Teller effect in CH_4^+ is very strong and leads to a stabilization energy of about 1.5 eV by distortion of the nuclear framework. The linear Jahn-Teller effect leads to minima of D_{2d} point-group symmetry by distortion along the bending mode ν_2 of e symmetry, or of C_{3v} symmetry by distortion along the two modes of f_2 symmetry (asymmetric C—H stretching mode ν_3 and C—H bending mode ν_4) [20,17]. The consideration of quadratic vibronic coupling terms can lead to further distortion and to equilibrium structures of C_{2v} symmetry [17,19]. The number of possible equivalent structures of a given symmetry corresponds to the ratio of the order of the CNPI group to the order of the point group considered, i.e., $48/24 = 2$ for tetrahedral structures (corresponding to the two enantiomers arising from numbering the hydrogen atoms from 1 to 4; the interconversion between the enantiomers corresponds to the unfeasible stereomutation of a chiral molecule [16]),

---

* Corresponding author.
   E-mail address: merkt@phys.chem.ethz.ch (F. Merkt).

$48/6 = 8$ for C_{3v} structures, $48/8 = 6$ for D_{2d} structures, and $48/4 = 12$ for C_{2v} structures.

The potential energy surfaces associated with the $\widetilde{X}^+$ $^2F_2$ electronic ground state of CH_4^+ have been characterized in numerous *ab initio* quantum-chemical studies (see, e.g., Refs. [21–29,19]). Since the work of Meyer [23], there is agreement that the minimum-energy structure has C_{2v} symmetry, with two long C–H bonds separated by a small angle and two short C—H bonds separated by a large angle. Paddon-Row et al. [24], Frey and Davidson [25], and Opalka and Domcke [19] have carried out detailed investigations of the potential energy surfaces of CH_4^+ and determined several of the essential structures, as depicted in Fig. 1. The twelve equivalent C_{2v} structures form two distinct enantiomeric sets. The topological connectivity of the different structures of each enantiomeric set is represented by an octahedron [24,25] in which the six equivalent C_{2v} structures are placed at the vertices, as illustrated in Fig. 1a. These structures, labeled 1–6 in Fig. 1a, are connected by low-lying C_s transition states along the edges of the octahedron. The centers of each face of the octahedron corresponds to C_{3v} structures. Four of these structures, labeled $C_{3v}(II)$ in Fig. 1c and marked by a red dot in Fig. 1a and b, have a doubly degenerate electronic ground state. The remaining four, labeled $C_{3v}(I)$ in Fig. 1c, have a nondegenerate ground state. The T_d and the three D_{2d} structures coincide with the center of the octahedron.

The low-energy barriers separating the C_{2v} equilibrium structures of each enantiomeric set lead to large amplitude tunneling motions along the edges of the octahedron that interconvert the different C_{2v} structures on the picosecond timescale and lead to tunneling splittings of about 16 cm^{-1} [30] that can be resolved in high-resolution photoelectron spectra. Cyclic sequences of such tunneling interconversion represent a type of large-amplitude motion referred to as pseudorotation, examples being the cyclic interconversion of the structures 1, 2 and 5, or the structures 1, 4 and 5 along the edges of a given face of the octahedron (see Fig. 1a). The treatment of such pseudorotations is essential to understand the spectrum of CH_4^+ at low energies [1,3]. When considering the pseudorotational motion of CH_4^+ without explicitly treating all three potential-energy sheets associated with the F_2 electronic state, it is necessary to explicitly introduce a geometric phase to account for the topology of the potential landscape. Pseudorotational motions that encircle a degenerate (nondegenerate) C_{3v} ground state are associated with a geometric phase of π (0) [3], as discussed in more general terms by, e.g., Herzberg and Longuet-Higgins [31]. In treatments of the Jahn-Teller effect that consider all three potential sheets of the F_2 electronic state, the geometric phase is implicitly accounted for. The remarkable effect of this geometric phase in the case of the electronic ground state of CH_4^+ is the modification of the structure and degeneracy of the lowest pseudorotation-tunneling levels from (a_1, f_2, e) for a phase of 0 to (f_2, f_1) for a phase of π, where the levels in parentheses are listed in order of increasing energy [30].

Experimental evidence for the C_{2v} equilibrium structure and the large-amplitude pseudorotational tunneling motion of CH_4^+ first came from studies of the electron-paramagnetic resonance (EPR) spectrum of CH_4^+ and its deuterated isotopomers in neon matrices [32–34]. Further evidence was provided by Coulomb-explosion experiments [35,36], but the latest analysis of the results of such experiments suggested the C_{2v} structures to be saddle points of the potential energy surfaces rather than minima [37,38]. Our approach to study the Jahn-Teller effect in CH_4^+ is by photoelectron spectroscopy of CH_4, which offers the advantage of obtaining the rovibronic level structure of the "isolated" molecules in the gas phase.

2. Review of previous photoelectron spectroscopic results and theoretical models

The experimental data available on the rovibrational energy-level structure of CH_4^+ and its deuterated isotopomers were obtained by PFI-ZEKE photoelectron spectroscopy in two distinct periods, as summarized in Refs. [1,3] for the first period and Refs. [4,5] for the second.

In the first set of studies, rotationally resolved single-photon PFI-ZEKE photoelectron spectra were obtained in the range 100,800–104,100 cm^{-1} for CH_4^+, 100,740–102,350 cm^{-1} for CDH_3^+, 101,810–102,200 cm^{-1} for $CD_2H_2^+$, and 102,090–102,490 cm^{-1} for CD_4^+ [2,39,1,3,40]. As example, the PFI-ZEKE photoelectron spectrum of CH_4 is depicted in Fig. 2. After the first band centered around 101,770 cm^{-1}, the density of lines becomes so high that no distinct vibronic band structure is recognizable.

The analysis of these spectra was based on a one-dimensional model of the pseudorotational motion connecting the C_{2v} equilibrium structures via C_s transition states [2,3]. Zero-point-energy-corrected minimum-energy paths connecting the three structures represented by the corners of each faces of the octahedron in Fig. 1a were derived. These paths represent pseudorotations that leave one of the C—H bonds unchanged and are referred to as pseudorotations around one of the C—H bonds. The eigenstates of the pseudorotational nuclear motion were computed for the different isotopomers by solving the one-dimensional nuclear Schrödinger equation. The one-dimensional nature of these paths prevented
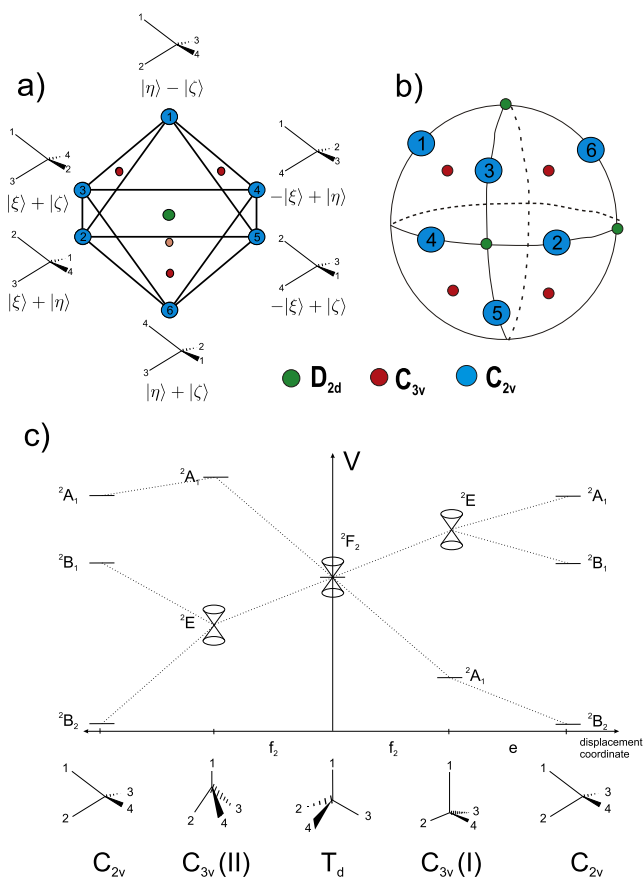

Fig. 1. (a) Topological representation of the connectivity of the six equivalent C_{2v} equilibrium structures of CH_4^+ in an octahedron. (b) Mapping of the $F \otimes (f \oplus e)$ Jahn-Teller effect of CH_4^+ onto the surface of a sphere. (c) Schematic representation of the relative energetic order of the different T_d, C_{2v}, and C_{3v} structures for the three components of the F_2 electronic ground state of CH_4^+. See text for details.
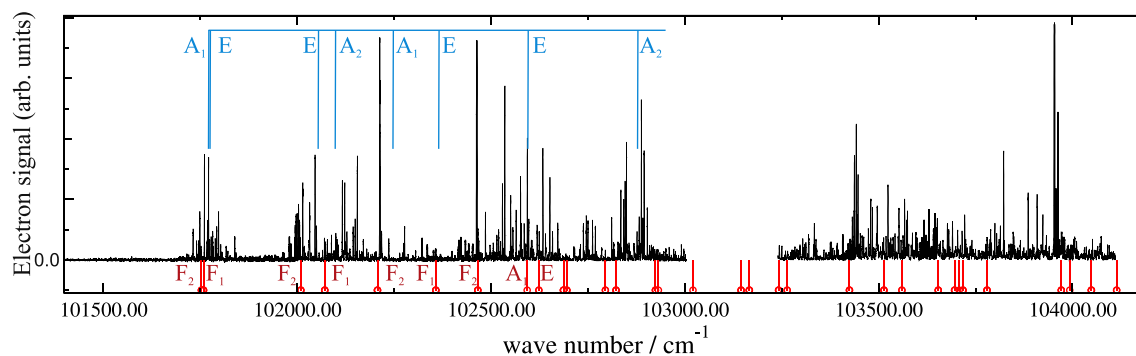
Fig. 2. (a) PFI-ZEKE photoelectron spectrum of CH_4 recorded by Signorell and Merkt [2]. The upper (blue) assignment bar gives the results of one-dimensional calculations of the pseudorotational motion of CH_4^+, as described in Refs. [2,3]. The lower (red) assignment bar gives the results of the two-dimensional treatment of the e and f_2 C—H bending modes described in Section 3 (adapted from Ref. [5]). See text for details. (For interpretation of the references to color in this figure legend, the reader is referred to the web version of this article.)

the derivation of symmetry labels in the T_d group for CH_4^+ but provided insights into the pseudo-rotational motion. The three equivalent minima in the case of CH_4^+ and CD_4^+ correspond to the situation encountered in internal-rotation problems involving methyl groups and lead to pairs of tunneling levels of A and E symmetry with tunneling splittings increasing with increasing energy, as given by the upper assignment bar in Fig. 2, which is taken from Ref. [2].

The experimental proof of the C_{2v} equilibrium structure of CH_4^+ came from the spectrum of the lowest band of the photoelectron spectrum of CD_2H_2 after realizing that the zero-point vibrational motion favors structures in which both D atoms are placed on short bonds and the H atoms on long bonds [39]. The lowest vibrational level is associated with a pseudorotational motion around a short C—D bond. The minimum of the one-dimensional pseudorotational path with the second D atom also on a short bond lies energetically lower than the other two minima, which each have one H atom on a short bond. Consequently, the ground vibrational level has its wavefunction localized in the minimum where the two D atoms occupy a short bond, and therefore has a rigid structure. The rotational structure could be assigned using a rigid-rotor model and the three rotational constants unambiguously proved the C_{2v} equilibrium structure [39].

Similar considerations for all isotopomers enabled the internally consistent interpretation of their vibronic structure at low energies [3]. An important insight was the realization that in CDH_3^+ the pseudorotation around a short C—D bond is energetically favored over the pseudorotation around a long C—D bond, whereas it is the pseudorotation around a long C—H bond that is favored in CD_3H^+. Bands associated with both types of pseudorotation could be assigned in the spectrum of CDH_3. Further results of this period were (i) semi-quantitative analyses of the rotational structure of CH_4^+ [40] and CD_4^+ [3], (ii) accurate values of the adiabatic ionization energies of CD_2H_2 (101 852.3(14) cm^{-1}) and CD_4 (102,197.1 (56) cm^{-1}) [3], and values of the tunneling splittings resulting from the pseudorotational motion that could explain the equivalence of the protons observed in EPR spectra [3].

In the second set of studies, the experimental data were extended by the single-photon PFI-ZEKE photoelectron spectra of $^{13}CH_4$ in the range 101,700–101,850 cm^{-1} [41] and CD_3H in the range 102,000–102,600 cm^{-1} [42]. In addition, double-resonance experiments with VUV and IR laser radiation (see Section 4 for details) were carried out in CH_4 to determine the nuclear-spin symmetries associated with the different lines of the origin band of the PFI-ZEKE photoelectron spectrum and the rotational quantum numbers of the initial rotational levels [30]. These

assignments provided the key to the rotational assignment of the lowest band of the photoelectron spectrum of CH_4.

The interpretation of the rotational structure was carried out in two steps [30,41]. In the first step, the pseudorotational motion interconverting the six equivalent C_{2v} structures of a given enantiomeric set was treated at low energies in a matrix representation of the tunneling problem using basis states

$$\phi_n = |n\rangle|\chi_n\rangle, \qquad n = 1\text{--}6 \qquad (1)$$

with vibrational wavefunctions $|\chi_n\rangle$ localized in the individual wells corresponding to the C_{2v} equilibrium structures. The adiabatic electronic wavefunctions $|n\rangle$ in these wells were obtained as eigenvalues of the potential-energy operator $U(\vec{Q})$ derived by Frey and Davidson [25] and are linear combinations of the three diabatic electronic functions ($|\xi\rangle$, $|\eta\rangle$, $|\zeta\rangle$) of the F_2 electronic ground state of CH_4^+, i.e., $\frac{1}{\sqrt{2}}(|\xi\rangle + |\eta\rangle)$, $\frac{1}{\sqrt{2}}(|\xi\rangle + |\zeta\rangle)$, $\frac{1}{\sqrt{2}}(-|\xi\rangle + |\eta\rangle)$, $\frac{1}{\sqrt{2}}(-|\xi\rangle + |\zeta\rangle)$, $\frac{1}{\sqrt{2}}(|\eta\rangle - |\zeta\rangle)$ and $\frac{1}{\sqrt{2}}(|\eta\rangle + |\zeta\rangle)$ [30] (see also Section 3). In the case of CH_4^+ and assuming that the vibrational functions in the different wells do not overlap, the vibronic (ev) tunneling matrix takes the form

$$\mathbf{H}_{ev} = \begin{pmatrix} E & \sigma & 0 & -\sigma & \sigma & \sigma \\ \sigma & E & -\sigma & 0 & -\sigma & \sigma \\ 0 & -\sigma & E & \sigma & \sigma & \sigma \\ -\sigma & 0 & \sigma & E & -\sigma & \sigma \\ \sigma & -\sigma & \sigma & -\sigma & E & 0 \\ \sigma & \sigma & \sigma & \sigma & 0 & E \end{pmatrix}, \qquad (2)$$

with $H_{nn} = H_{11} = E$ and tunneling coupling element σ, and has eigenvalues $E_{F_2} = E + 2\sigma$ and $E_{F_1} = E - 2\sigma$. Because σ is negative, the ground vibronic state of CH_4^+ has F_2 vibronic symmetry.

Similar tunneling matrices can be obtained for all isotopomers by considering that deuteration can change both the relative depth of the six wells and the value of the coupling elements [5]. For instance, the tunneling matrix for CDH_3^+ takes the form given in Eq. (24) of Ref. [5], which has eigenvalues

$$E_E = \frac{1}{2}(\sigma - \sigma' + \Delta - S), \qquad (3)$$

$$E_{A_2} = -2\sigma, \qquad (4)$$

$$E_{A_1} = -2\sigma' + \Delta, \qquad (5)$$

and

$$E_E = \frac{1}{2}(\sigma - \sigma' + \Delta + S), \qquad (6)$$

where $S = \sqrt{(\sigma + \sigma')^2 + 12\sigma''^2 - 2(\sigma + \sigma')\Delta + \Delta^2}$. Here, Δ is the energy difference between the well depths of the pseudorotations around a long and a short CD bond, and σ and σ' are the respective tunneling elements, and σ'' is the coupling element connecting the two types of structures. The first pair of tunneling levels (Eqs. (3) and (4)) is inverted because the corresponding pseudorotational motion is around a short C—D bond and encircles a C_{3v} structure with a degenerate ground state. The second pair of tunneling levels is regular and corresponds to a pseudorotation around a long C—D bond that encircles a C_{3v} structure with a nondegenerate ground state. This finding of two isomeric forms, with the D atom located either on a long ($CD_\ell H_3^+$) or a short ($CD_s H_3^+$) bond confirmed the earlier analysis with one-dimensional pseudorotational paths discussed above, but also established that the two species can be considered as isomers because the tunneling between them is suppressed. The analysis also enabled the determination of the tunneling splittings of $CD_\ell H_3^+$ and $CD_s H_3^+$ to be 6.6(5) cm^{-1} and 9.5 (6) cm^{-1}, respectively [42]. The sequence of the two pairs of tunneling levels is opposite in CD_3H^+ because the lowest tunneling pair arises from the pseudorotational motion around a short C—D bond and encircles a C_{3v} structure with a nondegenerate ground state. The further reduction of symmetry in $CD_2H_2^+$ even leads to three isomeric forms, which are, in order of increasing energy, $CD_sD_sH_\ell H_\ell^+$, $CD_sD_\ell H_s H_\ell^+$, and $CD_\ell D_\ell H_s H_s^+$, as discussed in detail in Refs. [5,43].

In a second step, the rotational structure was treated using a global inertial axis system (xyz) common to all six equivalent equilibrium structures and defined with respect to the reference tetrahedral geometry [30], by adapting a procedure originally introduced to treat the rotational motion of molecules in local-mode representation [44]. In this procedure, the equilibrium structures are obtained by distorting the reference structure, which involves elongating two C-H bonds and shortening the other two, changing the HCH angles, and moving the C atom up or down along one of the three axes of the global reference frame. Then, the global axis system is rotated so that it coincides with the principal-axis system of the distorted structure. For each C_{2v} structure, the rotational Hamiltonian is expressed as an asymmetric-top rigid-rotor Hamiltonian of the form

$$\frac{\widehat{H}^{\text{rot}}}{hc} = \frac{1}{2}(B + C)(\widehat{J}_x^2 + \widehat{J}_y^2) + \frac{1}{2}(B - C)\left(\widehat{J}_x\widehat{J}_y + \widehat{J}_y\widehat{J}_x\right) + A\widehat{J}_z^2. \quad (7)$$

The effective tunneling-rotation Hamiltonian in the basis of the eigenstates of Eq. (2) is

$$\widehat{H}_{\text{rve}} = U^T\widehat{H}^{\text{rot}}U + \widehat{H}_{\text{ve}}, \quad (8)$$

where $\widehat{H}^{\text{rot}}$ is a diagonal matrix of rotational operators of the form of Eq. (7) for the six C_{2v} local structures and U is the eigenvector matrix of $\mathbf{H}_{\text{ev}}$ (Eq. (2)). The tunneling-rotation eigenstates are obtained as eigenvalues and eigenfunctions of Eq. (8). This procedure, outlined here for CH_4^+ and CD_4^+, was adapted to also treat CDH_3^+ and CD_3^+H [42] and $CD_2H_2^+$ [43].

The main results of this second phase of studies were (i) the assignment of the rovibrational structure of the lowest and only distinct band of the PFI-ZEKE photoelectron spectra of CH_4 [30], (ii) the assignment of the rovibrational structure of the first few bands of the photoelectron spectra of all deuterated isotopomers of methane [41–43], and (iii) the derivation of the parameters of the effective rotation-tunneling Hamiltonian, i.e., the rotational constants A, B, and C, the tunneling coupling elements σ (σ', σ'') and improved values of the adiabatic ionization energies of $^{12}CH_4$ (101,752.2(15) cm^{-1} [41]), $^{13}CH_4$ (101,756.6(15) cm^{-1} [41]), CDH_3 (101,802.8(15) cm^{-1} [42]), CD_3H (102,021.4(20) cm^{-1} [42]) and CD_4 (102,196.9(15) cm^{-1} [41]).

The analyses of the photoelectron spectra carried out during the two phases are complementary, and each has its strengths and shortcomings. The one-dimensional treatment of the pseudorotational motion brought the advantages of being based on a model relying on *ab initio* calculations and thus of providing estimates of the tunneling splitting, but could not be used to derive the symmetry labels for CH_4^+ in the $T_d(M)$ molecular symmetry group nor to analyze the rotational structure of the fluxional isotopomers CH_4^+ and CDH_3^+. Pseudo-rotational motions connecting three of the six equivalent minima of CH_4^+ could be described, but the tunneling problem had to be artificially separated into two distinct calculations. The treatment of the tunneling-rotational structure with effective Hamiltonians permitted the derivation of symmetry labels in the T_d group and the assignment of the rotational structure but without relying on, or enabling comparison with, the results of ab initio calculations. More importantly, the treatment is intrinsically limited to the tunneling motion involving basis states located in the immediate vicinity of the C_{2v} equilibrium structures, i.e., basis states of the form given by Eq. (1) in their vibrational ground state. This limitation restricts the treatment to the lowest F_2 and F_1 vibronic levels of CH_4^+ and CD_4^+, to the lowest two pairs of (E,A) levels of CDH_3^+ and CD_3H^+, and to the six lowest levels (B_2, A_1, B_1, B_2, A_2 and B_1) of $CD_2H_2^+$, as explained in Refs. [43,5].

In the case of CH_4^+, overcoming these deficiencies necessitates experimental and theoretical work. Experimentally, the determination of the nuclear-spin symmetries associated with the lines of the PFI-ZEKE photoelectron spectrum located beyond the origin band would be required for comparison with the prediction of an improved model. Theoretically, the development of methods enabling the calculation of the pseudorotation-tunneling motion in at least two dimensions would be necessary to derive the symmetry of the tunneling levels in the T_d group. The remainder of this article describes progress in both directions.

3. Two-dimensional calculations of the pseudorotational-tunneling levels of CH_4^+

In standard treatments of the Jahn-Teller effect, the kinetic-energy term of the Hamiltonian describing the nuclear motion can be expressed as [18]

$$\widehat{H}_{\text{kin}} = \sum_{v_\gamma} -\frac{\hbar^2}{2\mu_v}\frac{\partial^2}{\partial Q_{v_\gamma}^2}\mathbf{1} \quad (9)$$

where μ_v is the reduced mass of the vibrational mode and $\mathbf{1}$ is the unit matrix. The potential-energy term, truncated to second order, is

$$V(\vec{Q}) = \sum_{v_\gamma}\left(\frac{1}{2}\mu_v\omega_v^2 Q_{v_\gamma}^2\mathbf{1} + V_v Q_{v_\gamma}\mathbf{C}_{v_\gamma} + K_v Q_{v_\gamma}^2\mathbf{1}\right), \quad (10)$$

where V_v and K_v are the linear and quadratic coupling constants, ω_v is the harmonic vibrational frequency of the vibrational mode v, and $\mathbf{C}_{v_\gamma}$ is a matrix of Clebsch-Gordan coefficients that can be found in tables [17,45]. In CH_4^+, the Jahn-Teller active modes are one e mode with C—H bending character, and two f_2 modes, one having C—H stretching character, the other bending character. The latter f_2 mode is known to be more active than the former [28,29,19].

Adiabatic potential energy surfaces $E_{\text{ad}}(\vec{Q})$ and electronic eigenstates $|a(\vec{Q})\rangle$ are obtained by solving

$$V(\vec{Q})|a(\vec{Q})\rangle = E_{\text{ad}}(\vec{Q})|a(\vec{Q})\rangle. \quad (11)$$

In the case of CH_4^+, the three adiabatic electronic states $|a(\vec{Q})\rangle = |x(\vec{Q})\rangle$, $|y(\vec{Q})\rangle$ and $|z(\vec{Q})\rangle$ arising from the F_2 ground state are linear combinations of the diabatic electronic states $|\xi(\vec{Q})\rangle, |\eta(\vec{Q})\rangle$ and $|\zeta(\vec{Q})\rangle$.

Retaining only the linear Jahn-Teller coupling terms, the potential energy operator for the $F \otimes (f \oplus e)$ problem can be expressed in the diabatic basis by

$$\widehat{V}(\vec{Q}) = \widehat{V}_0(\vec{Q}) + \begin{bmatrix} V_e\left(\frac{Q_{e'}}{2} - \frac{\sqrt{3}}{2}Q_{e''}\right) & -V_f Q_{f'''} & -V_f Q_{f''} \\ -V_f Q_{f'''} & V_e\left(\frac{Q_{e'}}{2} + \frac{\sqrt{3}}{2}Q_{e''}\right) & -V_f Q_{f'} \\ -V_f Q_{f''} & -V_f Q_{f'} & -V_e Q_{e'} \end{bmatrix},$$
(12)

where

$$\widehat{V}_0(\vec{Q}) = \sum_{v_\gamma} \left(\frac{1}{2}\mu_v \omega_v^2 Q_{v_\gamma}^2 \mathbf{1}\right).$$
(13)

In this section we describe a two-dimensional model of the Jahn-Teller effect in CH_4^+ that enables us to include the effects of the e and the f_2 bending modes by mapping the potential-energy landscape that results from these modes onto the surface of a sphere with the polar angle θ and the azimuthal angle ϕ. The f_2 asymmetric stretching mode is not included in this model. To map the $F \otimes (f \oplus e)$ Jahn-Teller effect onto a sphere, we follow a procedure similar to that introduced to treat the Jahn-Teller effect in systems displaying high symmetry, such as C_{60}^+ and icosahedral complexes (see Refs. [46,18] and references therein). The two components (e′ and e″) of the e C—H bending mode and the three components (f′, f″ and f‴) of the f_2 C—H bending mode are represented by the real-valued spherical harmonics with $\ell = 2$

$$Q_{e'} = d(3(\cos\theta)^2 - 1),$$
(14)

$$Q_{e''} = d\sqrt{3}(\sin\theta)^2 \cos(2\phi),$$
(15)

$$Q_{f'} = d\sqrt{3}\sin(2\theta)\sin\phi,$$
(16)

$$Q_{f''} = d\sqrt{3}\sin(2\theta)\cos\phi,$$
(17)

and

$$Q_{f'''} = d\sqrt{3}(\sin\theta)^2 \sin(2\phi),$$
(18)

where d is a distortion parameter that will be defined below. Pairs (θ, ϕ) of values of the polar and azimuthal angles correspond to specific distorted structures of CH_4^+. For instance, the three pairs $(0,0)$, $(\pi/2, 0)$, and $(\pi/2, \pi/2)$ only give non-vanishing contributions to the distortion from e components (i.e., from e′, e″, and a linear combination of e′ and e″, respectively) which lead to the three D_{2d} structures expected for a given enantiomeric set. These structures are marked by green dots in Fig. 1b. Similarly, the four C_{3v} structures correspond to $\theta_m = \pm 54.736°$ (the magic angle) and $\phi = \pm \pi/4$ and are indicated by the red dots in Fig. 1b. We note that this model only describes 4 C_{3v} structures within one enantiomeric set, although *ab initio* quantum chemical calculations predict 2×4 such structures [24,25], two of which are represented in Fig. 1b. This is the case because the f_2 stretching mode is not taken into account in the present model.

Using the two-dimensional parameterization of the five-dimensional coordinate space introduced in Eqs. (14)–(18), the wave function describing the lowest-lying adiabatic electronic surface can be expressed as a linear combination of the diabatic electronic functions as [46,18]

$$|z\rangle = \sin\theta \cos\phi |\xi\rangle + \sin\theta \sin\phi |\eta\rangle + \cos\theta |\zeta\rangle.$$
(19)

The corresponding electronic wave functions $|z(\theta, \phi)\rangle$ at the position of the D_{2d} structures are $|z(0,0)\rangle = |\zeta\rangle, |z(\pi/2, 0)\rangle = |\xi\rangle, |z(0, \pi/2)\rangle = |\eta\rangle$, at one of the C_{3v} structures it is $|z(\theta_m, \pi/4)\rangle = \frac{1}{\sqrt{3}}(|\xi\rangle + |\eta\rangle + |\zeta\rangle)$ and at one of the C_{2v} structures it is $|z(\pi/4, 0)\rangle = \frac{1}{\sqrt{2}}(|\xi\rangle + |\zeta\rangle)$.

In the special case corresponding to $\omega_e = \omega_f = \omega, \mu_e = \mu_f = \mu$ and $V_e^2/V_f^2 = 3/4$, the potential energy of the lowest adiabatic state $|z\rangle$ does not depend on θ nor on ϕ and can be represented by the isoenergetic surface $V(\theta, \phi) = V_0$ displayed in Fig. 3a. The pseudorotation in the space spanned by the e and f_2 bending modes is thus free with a constant distortion parameter $d = \frac{V_e}{2\mu\omega^2} = \frac{\sqrt{3}V_f}{4\mu\omega^2}$. The kinetic-energy operator of the pseudorotational motion becomes in this case

$$\widehat{H}_{kin} = -\frac{\hbar^2}{2\mu}\left(\frac{\partial^2}{\partial Q_{e'}^2} + \frac{\partial^2}{\partial Q_{e''}^2} + \frac{\partial^2}{\partial Q_{f'}^2} + \frac{\partial^2}{\partial Q_{f''}^2} + \frac{\partial^2}{\partial Q_{f'''}^2}\right)$$

$$= -\frac{\hbar^2 \mu \omega^4}{6V_e^2}\Delta_{\theta,\phi}.$$
(20)

In all other cases, the pseudorotational motion is hindered. However, the potential terms must still be totally symmetric in the T_d group, i.e., transform as A_1 in this group. Expanding the potential energy in a spherical-harmonics basis $Y_{\ell,m}(\theta, \phi)$ and retaining only terms of A_1 symmetry, one obtains

$$V = V_0 + \sqrt{\frac{7}{12}}\left[Y_{4,0} + \sqrt{\frac{5}{14}}(Y_{4,4} + Y_{4,-4})\right]V_4$$

$$+ \frac{1}{\sqrt{8}}\left[Y_{6,0} - \sqrt{\frac{7}{2}}(Y_{6,4} + Y_{6,-4})\right]V_6 + \dots.$$
(21)

The potential landscape arising from the first term in square brackets in Eq. (21) is depicted in Fig. 3b and has extrema located at the positions of the C_{3v} (blue) and D_{2d} (red) structures (compare with Fig. 1b). This situation corresponds to a purely linear Jahn-Teller effect. When V_4 is positive (negative), the Jahn-Teller stabilization energy resulting from the f_2 mode is larger (smaller) than that resulting from the e mode and the C_{3v} structure lies energetically below (above) the D_{2d} structure.

The lowest term in the expansion (21) that yields minimum-energy structures of C_{2v} symmetry is the $\ell = 6$ term. This term can therefore be considered to account in lowest order for the quadratic Jahn-Teller effect. It leads to potential-energy minima at the angle pairs $(\pi/4, 0)$, $(3\pi/4, 0)$, $(\pi/2, \pm\pi/4)$, and $(\pi/4, \pm\pi/2)$ corresponding to the structures 3, 5, 2, 4, 1 and 6 in Fig. 1a and b. From Eq. (19), one obtains the adiabatic electronic functions indicated in Fig. 1a for these structures.

The relevant structures (there are 3, 4 and 6 structures of D_{2d}, C_{3v}, and C_{2v} symmetry, respectively) have only been drawn on
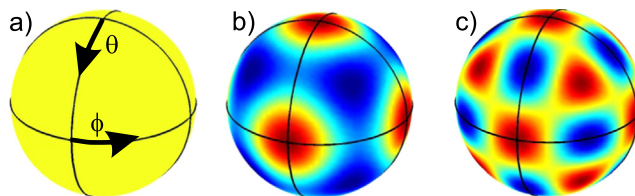

Fig. 3. (a) Potential energy of the lowest adiabatic state $|z\rangle$ as a function of the angles θ and ϕ for the special case corresponding to $\omega_e = \omega_f = \omega, \mu_e = \mu_f = \mu$ and $V_e^2/V_f^2 = 3/4$, for which $V(\theta, \phi) = V_0$. (b) Deviation of the potential energy from V_0 arising from the $\ell = 4$ term of the expansion (21) for a positive value of V_4. (c) Deviation of the potential energy from V_0 arising from the $\ell = 6$ term of the expansion (21) for a positive value of V_6. Blue corresponds to negative energies and red to positive energies. (For interpretation of the references to color in this figure legend, the reader is referred to the web version of this article.)

the front half of the sphere in Fig. 1b because the back half of the sphere is redundant for symmetry reasons. Indeed, inversion through the center changes the angle pair (θ, ϕ) into $(\pi - \theta, \pi + \phi)$ but does not change the value of the potential because it consists of only even-ℓ spherical harmonics, such that $V(\theta, \phi) = V(\pi - \theta, \pi + \phi)$. Inversion, however, changes the sign of the adiabatic electronic function $|z\rangle$ (see Eq. (19)). Single-valued vibronic functions can only be obtained if the pseudorotational wave functions also change sign upon inversion to compensate the sign change of the electronic wavefunctions. Consequently, they must be represented as linear combinations of odd-ℓ spherical harmonics.

To obtain the energetic positions of the vibronic levels of CH_4^+ in exploratory calculations using this two-dimensional model, the eigenvalues of

$$\widehat{H} = \widehat{H}_{kin} + V(\theta, \phi), \tag{22}$$

with $\widehat{H}_{kin}$ and V given by Eqs. (20) and (21), respectively, were determined using a basis of odd-ℓ spherical harmonics. We chose the free pseudo-rotation parameter $\hbar^2 \mu \omega^4/(6V_e^2)$ to be 10 cm^{-1} for CH_4^+, which corresponds to a Jahn-Teller stabilization energy of $E_{JT} = V_e^2/(2\mu\omega^2) = 2V_f^2/(3\mu\omega^2)$ of $12,700 \text{ cm}^{-1}$ for a harmonic wavenumber of 1235 cm^{-1}.
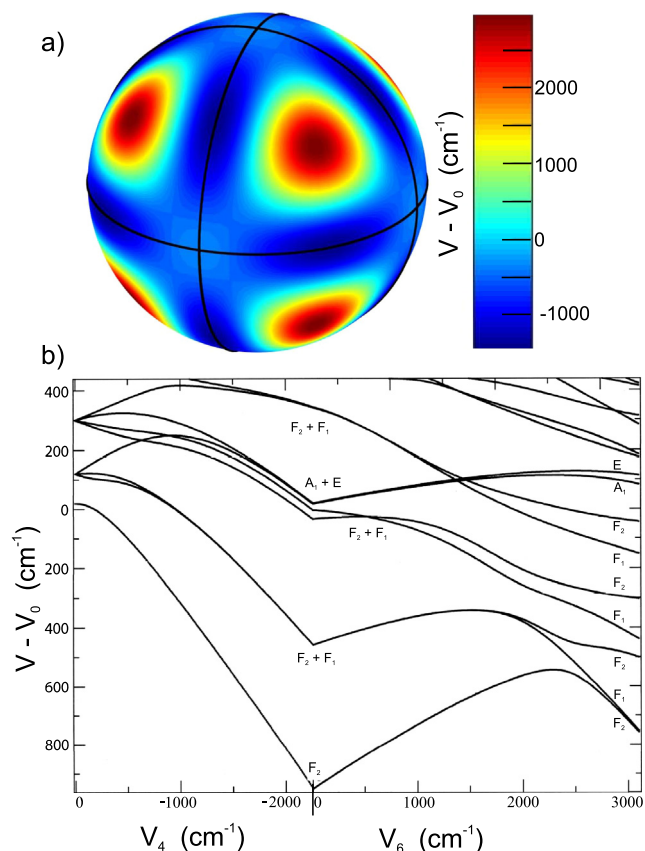

Fig. 4. (a) Potential energy of the electronic ground state of CH_4^+ as a function of the angles θ and ϕ (defined as in Fig. 3a) obtained with the values $V_4 = -2260 \text{ cm}^{-1}$ and $V_6 = 3100 \text{ cm}^{-1}$ determined from *ab initio* values of the potential energy of the D_{2d} (1100 cm^{-1}) and C_{3v} (4400 cm^{-1}) structures with respect to the potential energy of the C_{2v} equilibrium structures. (b) Correlation diagram illustrating how the vibronic levels evolve from the situation corresponding to a free pseudorotation ($V_4 = V_6 = 0$, left) via a situation where the linear Jahn-Teller effect favors the D_{2d} structure ($V_4 = -2260 \text{ cm}^{-1}$; $V_6 = 0$) to the situation corresponding to the potential surface depicted in panel (a).

Fig. 4b shows how the energy-level structure changes when V_4 is varied from 0 to -2260 cm^{-1} at $V_6 = 0$ (left panel), and then V_6 is increased from 0 to 3100 cm^{-1} at $V_4 = -2260 \text{ cm}^{-1}$ (right panel). The values $V_4 = -2260 \text{ cm}^{-1}$ and $V_6 = 3100 \text{ cm}^{-1}$ were determined so as to reproduce the *ab initio* values [24,25,47] of the approximate relative energetic positions of the D_{2d} (1100 cm^{-1}, second-order saddle point) and C_{3v} (4400 cm^{-1}, $C_{3v}(I)$ structure in Fig. 1c) structures with respect to the C_{2v} equilibrium structures.

The situation depicted on the very left of Fig. 4b corresponds to a free pseudorotation with odd-ℓ wavefunctions. The levels are $(2\ell + 1)$-fold degenerate and have vibronic symmetries F_2 ($\ell = 1$), $F_1 + F_2 + A_1$ ($\ell = 3$), $F_1 + 2F_2 + E$ ($\ell = 5$),..., as expected for $\ell = 2j + 1$ and integer values of the pseudorotation Jahn-Teller quantum number j ($j = 0, 1, 2, \ldots$).

At the very right of Fig. 4b, which corresponds to the vibronic structure of CH_4^+ predicted by our two-dimensional model, the minima of C_{2v} symmetry are deep so that the lowest tunneling doublet (F_1, F_2) is only split by 5.9 cm^{-1}. The F_2 level is the vibronic ground state, in agreement with the results of the calculations based on the effective tunneling model presented in Section 2. The two-dimensional treatment of e and f_2 C—H bending modes now also enables the prediction of the level structure, including vibronic symmetries in the T_d group, at higher energies.

The potential surface corresponding to the values of -2260 cm^{-1} for V_4 and 3100 cm^{-1} for V_6, shown in Fig. 4a, displays first-order saddle points of C_s symmetry located 955 cm^{-1} above the C_{2v} minima. One of these saddle points is located at $\theta = 0.264$ rad and $\phi = \pi/4$ and connects the two C_{2v} structures labeled 3 and 6 in panels a and b of Fig. 1. This result is in semi-quantitative agreement with *ab initio* calculations [24,25,47,19], which all predict the first-order saddle points of C_s symmetry to be located below, but close to, the second-order D_{2d} saddle points. This agreement is encouraging because no information on the energetic position of the C_s saddle points was used in the determination of the values of V_4 and V_6.

The positions of the vibronic levels calculated with this model are indicated along the lower assignment bar in Fig. 2, where they can be compared to the predictions made on the basis of the one-dimensional pseudorotational model reviewed in Section 2 and given along the upper assignment bar. The splitting of the lowest pair of tunneling levels (F_2 and F_1) we obtain is 5.9 cm^{-1}, which is larger than that obtained from the one-dimensional calculations (3.6 cm^{-1} [3]), but smaller than the value of 16.4 cm^{-1} [30] determined from the analysis of the rotational structure of the PFI-ZEKE photoelectron spectrum using the effective tunneling model based on Eqs. (2), (7) and (8). The calculations predict a higher density of vibronic states than the one-dimensional calculations and nicely accounts for the fact that only the lowest band of the PFI-ZEKE photoelectron spectrum is separated from the other bands by more than the width of the rotational structure of the lowest band.

The merits of the model presented in this section are (1) to provide a framework to predict the pseudorotational level structure by including e and f_2 modes explicitly, i.e., *five* vibrational degrees of freedom, (2) to predict vibronic eigenstates in the T_d symmetry group which implicitly include the effects of the geometric phase, and (3) to be based on parameters that can be taken from, or compared to, the results of *ab initio* quantum-chemical calculations.

Quantitatively accurate results cannot be expected from the calculations presented here because the model does not account for the effects of the a_1 and f_2 stretching modes, includes the quadratic Jahn-Teller coupling only in the lowest-order approximation, neglects bilinear and higher-order coupling terms and assumes an effective reduced mass for the pseudorotational motion that is not dependent on θ nor on ϕ. In addition, our calculations have disregarded contributions to the potential energy arising from

$\ell = 8, 10, \ldots$ terms in Eq. (21). These additional terms could be used to achieve a more quantitative representation of the potential-energy surfaces of CH_4^+. However, the deviation of the true vibrational frequencies, reduced masses and Jahn-Teller coupling parameters from the assumed equalities ($\omega_e = \omega_f = \omega$, $\mu_e = \mu_f = \mu$ and $V_e^2/V_f^2 = 3/4$) would also need to be accounted for.

4. Experimental procedure

This section describes the procedure followed to determine the nuclear-spin symmetry and the rotational quantum number of the initial level of CH_4 associated with lines of the PFI-ZEKE photoelectron spectrum located beyond the origin band. The experiments were carried out as described in Ref. [41] and relied on double-resonance threshold-ionization spectroscopy using pulsed mid-infrared and vacuum-ultraviolet laser radiation generated by non-linear optical techniques from the outputs of Nd:YAG-pumped dye lasers (repetition rate 25 Hz, pulse length ≈8 ns). The VUV laser radiation of wavenumber $\tilde{v}_{VUV} = 2\tilde{v}_1 + \tilde{v}_2$ was generated by resonance-enhanced sum-frequency mixing in Xe using the $(5p)^6 \rightarrow (5p)^5\ 6p[1/2]_0$ two-photon resonance of Xe at $2\tilde{v}_1 = 80{,}118.9839\ cm^{-1}$ [2]. The mid-infrared radiation of wavenumber $\tilde{v}_{IR} = \tilde{v}_{YAG} - \tilde{v}_{VIS}$ was produced by difference-frequency mixing of the outputs of the injection-seeded Nd:YAG laser and a dye laser in a potassium-titanyle-arsenate (KTA) crystal [30].

The IR and VUV laser pulse energies were typically 1 mJ and 1 nJ, and their bandwidth were 0.03 cm^{-1} and 0.5 cm^{-1}, respectively. The wavenumbers of all lasers used as input to the nonlinear frequency-conversion processes were calibrated at an accuracy of 0.03 cm^{-1} using a wavelength meter. The accuracy of the VUV and IR wavenumbers are estimated to be 0.2 cm^{-1} and 0.03 cm^{-1}, respectively.

The transitions from the rotational levels of the ground $\tilde{X}\ ^1A_1$ electronic state of CH_4 to the rovibronic levels of CH_4^+ were recorded using the techniques of PFI-ZEKE photoelectron spectroscopy [48] and MATI spectroscopy [49] by monitoring the field-ionization yield of high Rydberg states located below the rovibronic ionization thresholds using sequences of pulsed electric fields. To record the PFI-ZEKE photoelectron spectra, we used a two-pulse sequence consisting of a discrimination pulse of 130 mV/cm and a field-ionization pulse of −500 mV/cm. Larger discrimination (−330 mV/cm) and field-ionization (116.6 V/cm) pulses were employed to record the MATI spectra. To obtain the wavenumber of the field-free ionization thresholds, the field-induced shifts were corrected using the procedure described in Ref. [50], which resulted in a contribution of 0.3 cm^{-1} to the overall uncertainties of 0.5 cm^{-1} for thresholds measured by PFI-ZEKE and 1.5 cm^{-1} for those measured by MATI spectroscopy.

The gas sample was produced by expanding a spectroscopic-purity-grade CH_4 gas sample into vacuum using a pulsed valve generating a supersonic expansion. The rotational constant of CH_4 is large so that the sample probed experimentally primarily consisted of the $J = 0$ (A nuclear-spin symmetry), $J = 1$ (F nuclear-spin symmetry) and $J = 2$ (E and F nuclear-spin symmetry) ground-state levels. The two centrifugal components of the $J = 2$ level could be resolved in the IR spectrum of the fundamental band of the asymmetric C—H stretching mode v_4, as shown in Fig. 5. This spectrum was recorded by monitoring the CH_4^+ ions produced by VUV photoionization of the final states of the IR transitions.

We used the transitions of this IR spectrum to assign the nuclear-spin symmetry of the transitions in the threshold-ionization spectra using the two double-resonance schemes already exploited in Ref. [41]. In both schemes, the VUV laser pulse was delayed by about 1 μs with respect to the IR laser pulse to avoid ionization of the Rydberg states by the IR laser.

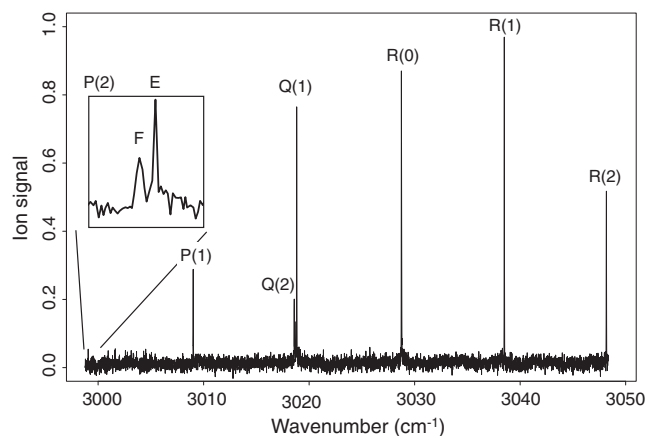**Fig. 5.** IR spectrum of the 4_0^1 band of CH_4 recorded by monitoring the CH_4^+ signal generated by $(1_{IR} + 1_{VUV})$ photoionization as a function of the IR-laser wavenumber. The VUV wavenumber was kept fixed at a position located slightly below the onset of the CH_4^+ signal in the single-photon VUV photoionization spectrum to suppress the background ionization signal. The intensity scale has been normalized to the intensity of the R(1) line.

In the first scheme, the wavenumber of the IR-laser is kept fixed at the position of one of the transitions of Fig. 5 to select a given nuclear-spin symmetry and rotational level, and the wavenumber of the VUV laser is scanned. As long as the VUV wavenumber is below the onset of single-photon VUV ionization, the only mechanism for the production of CH_4^+ is $(1_{IR} + 1_{VUV})$ resonance-enhanced two-photon ionization. When the VUV wavenumber is larger than the onset of single-photon ionization, the CH_4^+ ion yield consists of two contributions: single-photon ionization from any of the $J = 0-2$ ground-state rotational levels and $(1_{IR} + 1_{VUV})$ resonant two-photon ionization via the selected rotational state of the 4^1 vibrational level.

In the second scheme, the VUV wavenumber is kept fixed at the position of a selected line of the single-photon PFI-ZEKE photoelectron or MATI spectrum and the IR-laser wavenumber is scanned through the transitions of the 4_0^1 band displayed in Fig. 5. The observation of an intensity depletion of the selected line of the PFI-ZEKE photoelectron spectrum at an IR wavenumber corresponding to a line of the 4_0^1 band indicates that both lines have the same initial state, which enables one to assign the nuclear-spin symmetry and the rotational quantum number of the initial rotational level.

Typical examples of spectra recorded with the second scheme are depicted in Fig. 6, which shows how the PFI-ZEKE photoelectron signal varies as the IR laser wavenumber is scanned through the R(0) (panels (a) and (c)) and R(1) (panels (b) and (d)) lines of the 4_0^1 band of CH_4. Whereas in two cases (panels (a) and (b)) a depletion of the photoelectron signal is observed at the position of the IR transitions, as expected, an enhancement of the photoelectron signal is observed in the other two cases (panels (c) and (d)). We attribute this enhancement to an "accidental" transition from the selected rotational level of the 4^1 vibrational state of CH_4 to an excited rovibrational level of CH_4^+ located about 3000 cm^{-1} above the ground state of CH_4^+.

To confirm this interpretation of the enhancement of PFI-ZEKE photoelectron signal, we recorded PFI-ZEKE photoelectron spectra without simultaneous irradiation with the IR laser (full line in Fig. 7) and with the IR laser turned on and its wavenumber tuned to the position of the R(0) line of the 4_0^1 band of CH_4 (dashed line in Fig. 7). The four possible intensity behaviors are represented by the
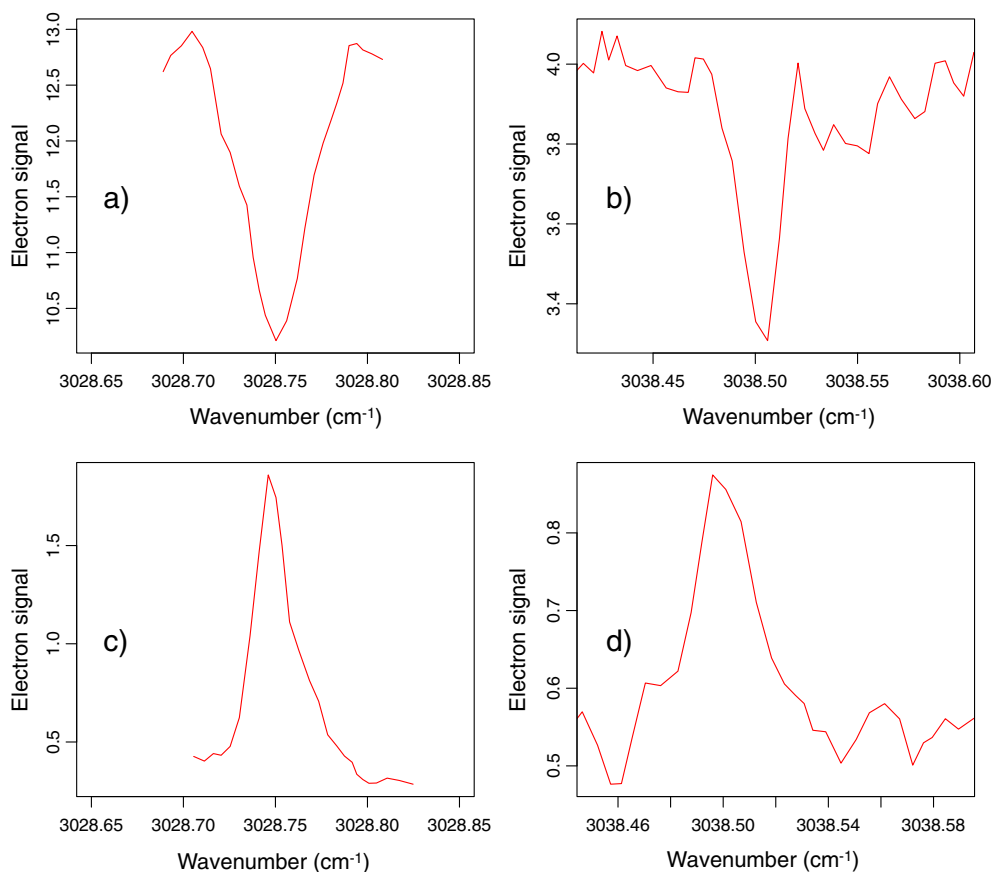
Fig. 6. Panels (a)–(d): PFI-ZEKE photoelectron signal (arb. units) recorded as a function of the wavenumber of the IR laser after fixing the VUV laser wavenumber at the positions marked a, b, c, and d, respectively, below the top trace of Fig. 8. In the case of panels (a) and (c), the IR laser was scanned through the R(0) line of the 4_0^1 band of CH_4 and in the case of panels (b) and (d) it was scanned through the R(1) line.

Fig. 7. Comparison of the VUV-PFI-ZEKE photoelectron spectra of CH_4 recorded with IR laser turned off (solid line) and with IR laser turned on and tuned to the R(0) line of the 4_0^1 band of CH_4 (dashed line). The labels 1–4 indicate the four intensity behaviors discussed in the text.
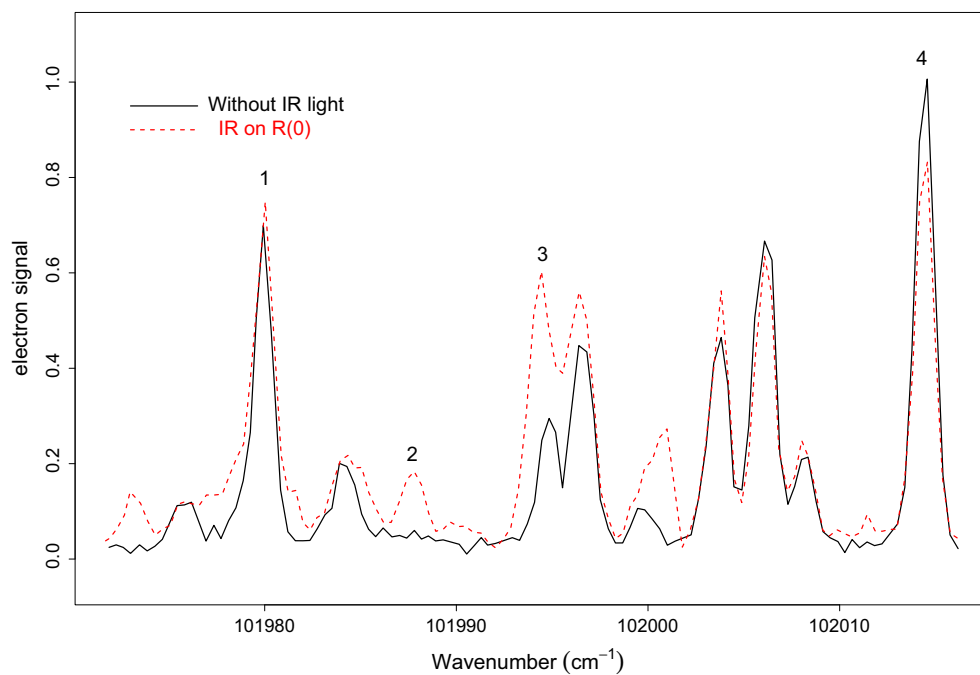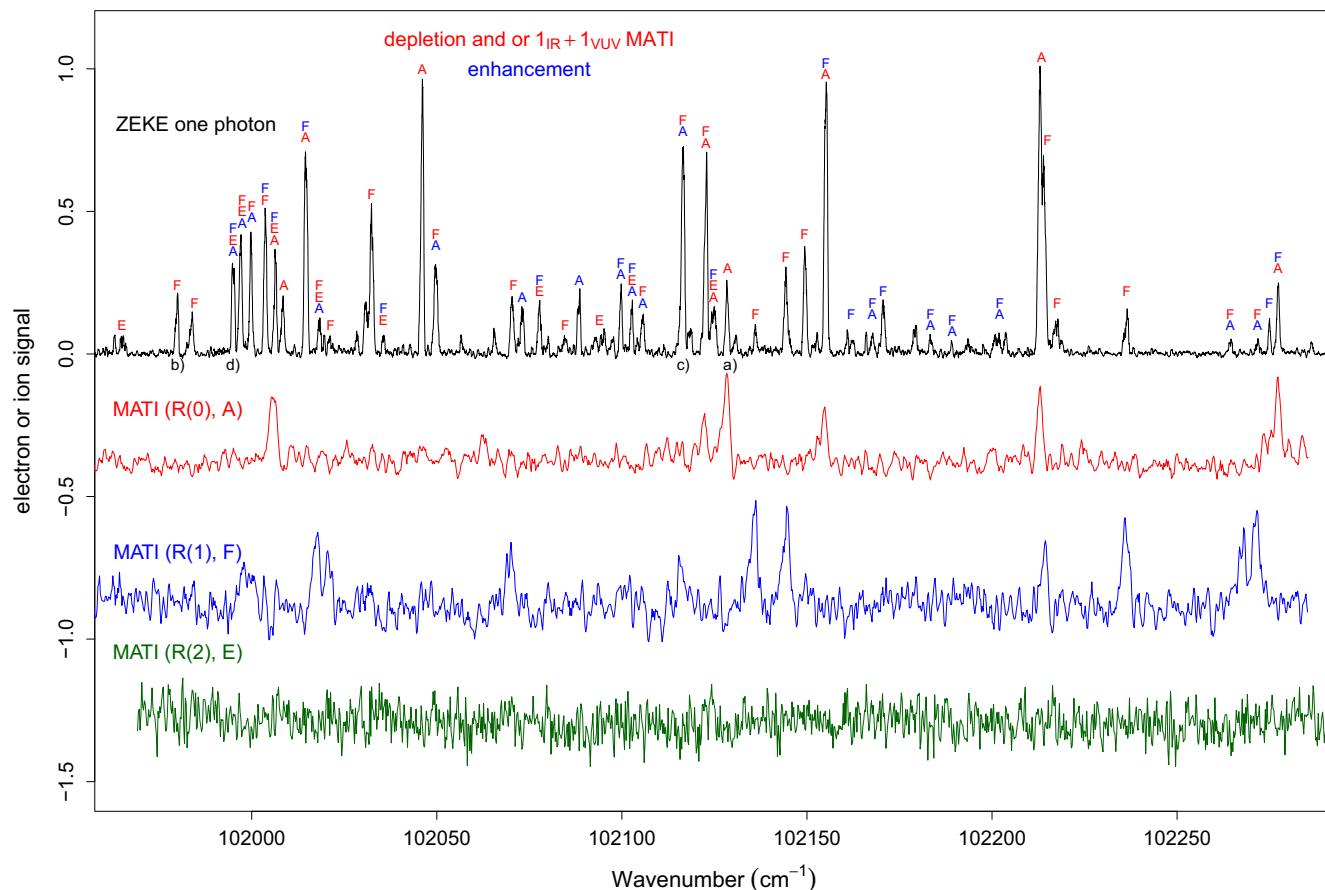
Fig. 8. Overview of the single-photon PFI-ZEKE photoelectron spectrum of CH_4 (top trace) and of the $(1_{IR} + 1_{VUV})$ MATI spectra of CH_4 recorded via the 4^1 $J = 1$ (second trace from the top), $J = 2$ (second trace from the bottom) and $J = 3$ (bottom trace) intermediate levels in the region from 101,950 to 102,300 cm^{-1}. The nuclear-spin symmetries indicated in red above the top trace were determined from $(1_{IR} + 1_{VUV})$ MATI spectra or by monitoring a depletion of the single-photon PFI-ZEKE line intensities caused by the IR laser. The nuclear-spin symmetries given in blue indicate an enhancement of the PFI-ZEKE photoelectron signal and thus transitions to levels located ≈ 3000 cm^{-1} beyond the origin band. (For interpretation of the references to color in this figure legend, the reader is referred to the web version of this article.)

lines marked 1–4 in Fig. 7. The lines marked 2, 3 and 4 correspond to lines involving levels of A nuclear-spin symmetry. The lines 3 and 4 are subject to the enhancement and depletion mechanisms discussed above, respectively. Line 2 is a photoionizing transition originating from the $J = 1$ level of the 4^1 state. Finally, line 1 involves CH_4 levels of E or F nuclear-spin symmetry and is not influenced by the IR laser when its wavenumber is resonant with the R(0) transition (A nuclear-spin symmetry). Whereas the observation of a depletion provides the symmetry assignments of the CH_4^+ levels located at the position above the initial neutral state given by the VUV wavenumber, the observation of an enhancement provides the symmetry assignments of CH_4^+ levels located about 3000 cm^{-1} higher.

Surprisingly, of all the cases where a change of intensity of the PFI-ZEKE photoelectron signal could be observed, more than half corresponded to an intensity enhancement. Moreover, this ratio was found to rapidly increase with increasing VUV wavenumber, making the observation of intensity depletion very rare at VUV wavenumbers beyond 102,200 cm^{-1}. This observation indicates that the signal-enhancement mechanism by $(1_{IR} + 1_{VUV})$ rapidly starts to dominate over the depletion mechanism as the VUV wavenumber increases beyond the adiabatic ionization threshold and that the density of states of CH_4^+ is already very high at an internal excitation of 3000 cm^{-1} above the ground state.

5. Experimental results

The double-resonance spectra recorded in the present study are displayed in Figs. 8 and 9. They extend the data reported on the origin band ($T_{CH_4^+} = 0$–90 cm^{-1}) in Ref. [41] and provide information on three distinct spectral regions of CH_4^+:

1. The region from the adiabatic ionization energy ($T_{CH_4^+} = 0$ cm^{-1}) to $T_{CH_4^+} = 600$ cm^{-1}. In this region (see Fig. 8), the assignments of nuclear-spin symmetry were obtained by monitoring the depletion of the intensity of the lines in the PFI-ZEKE photoelectron spectrum, as illustrated in Fig. 6a and b and from the $(1_{IR} + 1_{VUV})$ resonance-enhanced MATI spectra using the infrared radiation to select transitions from $J = 0$ (A), $J = 1$ (F) and $J = 2$ (E) ground-state levels (see red, blue and green traces in Fig. 8, respectively). To compare the single-photon PFI-ZEKE photoelectron spectrum and the MATI spectra in Figs. 8 and 9, the MATI spectra have been shifted by the corresponding IR transition wavenumbers.

2. The region $T_{CH_4^+} = [1700, 3000$ cm$^{-1}]$. In this region (see Fig. 9), the measurement of depletion of the lines of the PFI-ZEKE photoelectron spectrum was not attempted for the reasons mentioned in Section 4. The nuclear-spin symmetry was therefore only derived from the $(1_{IR} + 1_{VUV})$ resonance-enhanced MATI spectra depicted in Fig. 9.
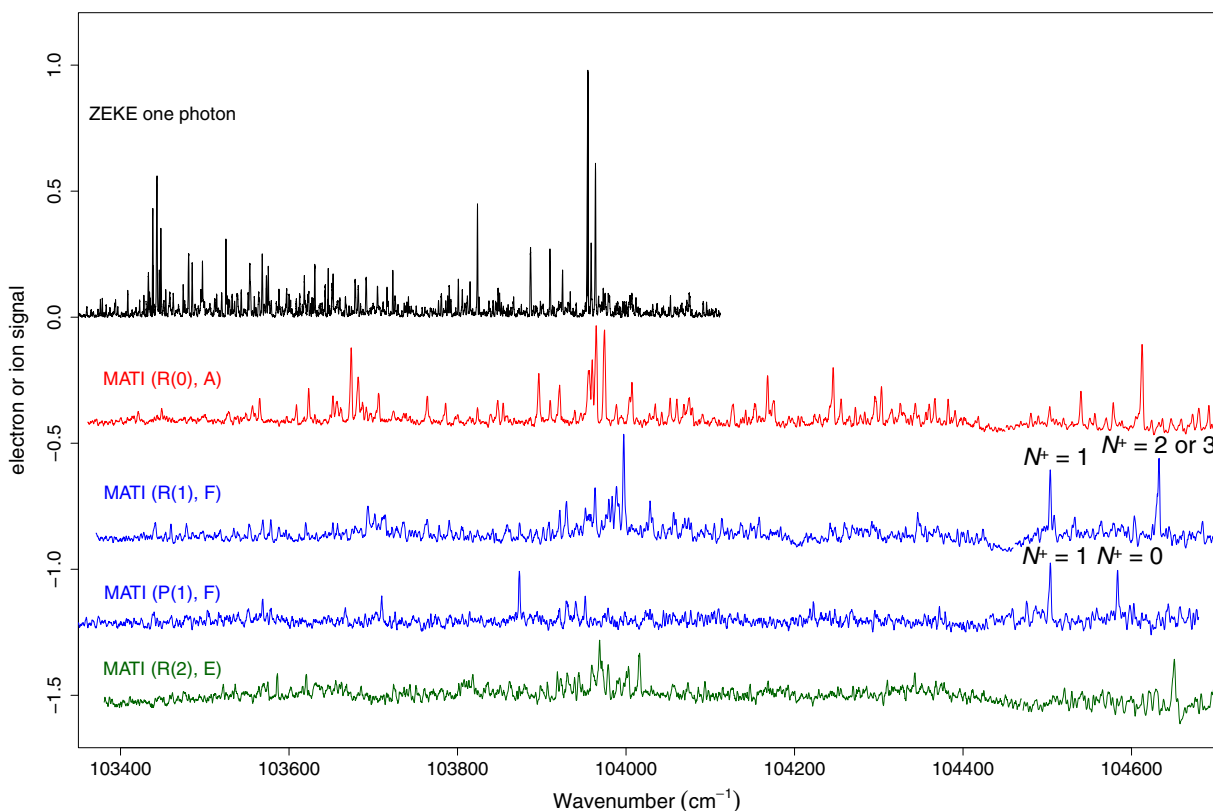
Fig. 9. Overview of the single-photon PFI-ZEKE photoelectron spectrum of CH_4 (top trace) and of the $(1_{IR} + 1_{VUV})$ MATI spectra of CH_4 recorded via the $J = 1(A)$ (second trace from the top), $J = 2(F)$ (third trace from the top), $J = 0(F)$ (second trace from the bottom) and $J = 3(E)$ (bottom trace) levels of the 4^1 vibrational level of CH_4^+ in the region from 103,400 to 104,650 cm^{-1}.

3. The region $T_{CH_4^+} = [3000, 3600 \text{ cm}^{-1}]$. In this region, the assignment of the nuclear-spin symmetry was determined from the enhancement of the intensity of the lines of the PFI-ZEKE photoelectron spectrum resulting from the IR laser, as explained in Section 4, see, e.g., the lines designated 2 and 3 in Fig. 7, or Fig. 6c and d.

The nuclear-spin symmetry assignments made for regions 1 and 3 are presented by the letters A, E and F placed above the corresponding lines of the PFI-ZEKE photoelectron spectrum (top trace in Fig. 8). The letters in red indicate the assignments for region 1 and those in blue indicate the assignments for region 3. The absolute positions of the ionic levels with respect to the neutral ground state were obtained by adding the ground-state rotational energy to the field-corrected positions of the PFI-ZEKE photoelectron lines, and in the case of region 3 also the IR wavenumber. These positions are listed in the columns labeled T in Table 1. The term values of the ionic levels, obtained as differences to the CH_4^+ rovibronic ground state of F_2 nuclear spin symmetry [41], are given in the columns labeled $T_{CH_4^+}$.

In region 2, the assignment of nuclear-spin symmetry directly results from the selected IR transitions, as indicated above the MATI spectra on the left of Fig. 9. The positions of the corresponding ionic levels are also given in Table 1.

The CH_4^+ energy levels listed in Table 1 were all accessed from the $J = 0$ (A), $J = 1$ (F) and $J = 2$ (E) rotational levels of the ground vibronic state of CH_4 in either one-photon or two-photon transitions. Single-photon ionization from the vibronic ground state of CH_4 to the ground electronic state of CH_4^+ is accompanied by small changes $\Delta N = N^+ - N \leqslant 1$ of the rotational angular-momentum quantum number [41,2]. Consequently, the angular-momentum quantum numbers of the ionic levels listed in Table 1 have values of $N^+ \leqslant 3$.

In favorable cases, the comparison of $(1_{IR} + 1_{VUV})$ two-photon MATI spectra recorded from the $J = 1$ (F_1) ground state level to $J = 0$ and $J = 2$ (F_2) levels of the 4^1 state via P(1) and R(1) IR-transitions enables one to determine the N^+ value of the ionic level. The 4^1 ($N = 0$) and 4^1 ($N = 2$) levels provide access to ionic levels with $N^+ = 0, 1$ and $N^+ = 1-3$ respectively. Lines observed in both spectra thus involve ionic levels with $N^+ = 1$, those observed only from the 4^1 ($N = 0$) level involve $N^+ = 1$ ionic levels and those observed from the 4^1 ($N = 2$) level involve $N^+ = 2, 3$ ionic levels. A good example of a spectral region where such assignments are possible is between 104,480 and 104,650 cm^{-1} in Fig. 9. The spacings between the levels that could be assigned in this manner are, however, too large to only represent rotational contributions.

When comparing the MATI with the PFI-ZEKE photoelectron spectra in Figs. 8 and 9, several aspects are striking. First, the PFI-ZEKE photoelectron spectrum consists of many more transitions than the MATI spectra combined. Second, the intensity distributions differ markedly. For instance, the MATI spectra do not reveal any transitions in the regions [102,075–102,110 cm^{-1}] and [102,160–102,210 cm^{-1}] in Fig. 8, and [103,400–104,600 cm^{-1}] in Fig. 9 whereas many lines are observed in these regions in the PFI-ZEKE photoelectron spectrum. Consequently, these regions contain fewer lines with nuclear-spin-symmetry assignments. Third, no transitions involving levels of E nuclear-spin symmetry could be detected in the MATI spectrum of Fig. 8. These differences may be explained by the different Franck-Condon factors, the different selection rules and the fact that some ground-state rotational levels with $J > 2$ might have been weakly populated under the conditions used to record the PFI-ZEKE photoelectron

Table 1
Term values and nuclear-spin symmetry of low-lying rovibronic levels of CH_4^+ determined in double-resonance experiments. T stands for the position of the energy levels with respect to the rovibronic ground state of CH_4. $T_{CH_4^+}$ represents these positions with respect to the rovibronic ground state of CH_4^+.

Γ_{rve}^+	$\bar{\nu}$, cm^{-1}	T, cm^{-1}	$T_{CH_4^+}$, cm^{-1}	Γ_{rve}^+	$\bar{\nu}$, cm^{-1}	T, cm^{-1}	$T_{CH_4^+}$, cm^{-1}
A	101761.9	101761.9	9.7	A	101779.1	101779.1	26.9
A	101784.8	101784.8	32.6	A	101798.2	101798.2	46.0
A	101806.9	101806.9	54.7	A	101817.7	101817.7	65.5
A	101840.4	101840.4	88.2	A	102007.7	102007.7	255.5
A	102009.7	102009.7	257.5	A	102015.8	102015.8	263.6
A	102047.4	102047.4	295.2	A	102124.0	102124.0	371.8
A	102126.0	102126.0	373.8	A	102129.6	102129.6	377.4
A	102156.4	102156.4	404.2	A	102214.2	102214.2	462.0
A	102278.8	102278.8	526.6	A	103421.0	103421.0	1668.8
A	103448.9	103448.9	1696.7	A	103527.9	103527.9	1775.7
A	103557.0	103557.0	1804.8	A	103565.2	103565.2	1813.0
A	103608.6	103608.6	1856.4	A	103623.4	103623.4	1871.2
A	103652.0	103652.0	1899.8	A	103657.0	103657.0	1904.8
A	103661.5	103661.5	1909.3	A	103673.6	103673.6	1921.4
A	103681.9	103681.9	1929.7	A	103688.6	103688.6	1936.4
A	103706.2	103706.2	1954.0	A	103723.8	103723.8	1971.6
A	103736.8	103736.8	1984.6	A	103764.0	103764.0	2011.8
A	103785.3	103785.3	2033.1	A	103799.3	103799.3	2047.1
A	103814.8	103814.8	2062.6	A	103823.7	103823.7	2071.5
A	103839.5	103839.5	2087.3	A	103847.5	103847.5	2095.3
A	103854.1	103854.1	2101.9	A	103858.3	103858.3	2106.1
A	103896.4	103896.4	2144.2	A	103910.0	103910.0	2157.8
A	103920.8	103920.8	2168.6	A	103939.0	103939.0	2186.8
A	103956.9	103956.9	2204.7	A	103960.0	103960.0	2207.8
A	103964.4	103964.4	2212.2	A	103974.2	103974.2	2222.0
A	103988.2	103988.2	2236.0	A	104005.7	104005.7	2253.5
A	104032.7	104032.7	2280.5	A	104052.3	104052.3	2300.1
A	104060.2	104060.2	2308.0	A	104073.2	104073.2	2321.0
A	104090.8	104090.8	2338.6	A	104104.0	104104.0	2351.8
A	104126.6	104126.6	2374.4	A	104142.0	104142.0	2389.8
A	104152.9	104152.9	2400.7	A	104168.0	104168.0	2415.8
A	104174.5	104174.5	2422.3	A	104193.4	104193.4	2441.2
A	104197.1	104197.1	2444.9	A	104204.5	104204.5	2452.3
A	104208.4	104208.4	2456.2	A	104224.0	104224.0	2471.8
A	104229.6	104229.6	2477.4	A	104244.7	104244.7	2492.5
A	104255.0	104255.0	2502.8	A	104264.8	104264.8	2512.6
A	104272.2	104272.2	2520.0	A	104278.3	104278.3	2526.0
A	104283.3	104283.3	2531.1	A	104295.8	104295.8	2543.6
A	104303.0	104303.0	2550.8	A	104314.6	104314.6	2562.4
A	104326.8	104326.8	2574.6	A	104343.8	104343.8	2591.6
A	104358.7	104358.7	2606.5	A	104366.5	104366.5	2614.0
A	104382.3	104382.3	2630.1	A	104390.4	104390.4	2638.2
A	104397.4	104397.4	2645.2	A	104401.9	104401.9	2649.7
A	104417.9	104417.9	2665.7	A	104480.5	104480.5	2728.3
A	104503.3	104503.3	2751.1	A	104539.8	104539.8	2787.6
A	104550.7	104550.7	2798.5	A	104556.5	104556.5	2804.3
A	104569.8	104569.8	2817.6	A	104578.5	104578.5	2826.3
A	104609.9	104609.9	2857.7	A	104632.5	104632.5	2880.3
A	104636.6	104636.6	2884.4	A	104647.4	104647.4	2895.2
A	104658.3	104658.3	2906.1	A	104671.6	104671.6	2919.4
A	104679.7	104679.7	2927.5	A	104691.5	104691.5	2939.3
A	105006.3	105006.3	3254.1	A	105010.1	105010.1	3257.0
A	105025.0	105025.0	3272.8	A	105027.0	105027.0	3274.8
A	105029.8	105029.8	3277.6	A	105033.6	105033.6	3281.4
A	105037.8	105037.8	3285.6	A	105048.3	105048.3	3296.1
A	105079.8	105079.8	3327.6	A	105095.6	105095.6	3343.4
A	105103.2	105103.2	3351.0	A	105118.5	105118.5	3366.3
A	105129.8	105129.8	3377.6	A	105132.7	105132.7	3380.5
A	105135.7	105135.7	3383.5	A	105146.4	105146.4	3394.2
A	105197.8	105197.8	3445.6	A	105213.4	105213.4	3461.2
A	105219.2	105219.2	3467.0	A	105232.0	105232.0	3479.8
A	105294.5	105294.5	3542.3	A	105301.7	105301.7	3549.5
A	105351.8	105351.8	3599.6				
E	101732.7	101763.1	11.9	E	101747.3	101778.7	26.5
E	101750.3	101781.7	29.5	E	101768.5	101799.9	47.7
E	101772.7	101804.1	51.9	E	101783.2	101814.6	62.4
E	101807.1	101838.5	86.3	E	101966.4	101997.8	245.6
E	101996.2	102027.6	275.4	E	101998.2	102029.6	277.4
E	102007.7	102039.1	286.9	E	102019.5	102050.9	298.7
E	102036.8	102068.2	316.0	E	102078.8	102210.2	358.0
E	102096.0	102127.4	375.2	E	102103.9	102135.3	383.1
E	102126.0	102157.4	405.2	E	103521.7	103553.1	1800.9
E	103536.2	103567.6	1815.4	E	103564.1	103595.5	1843.3

Table 1 (continued)

Γ_{rve}^{+}	$\bar{v}$, cm^{-1}	T, cm^{-1}	$T_{\text{CH}_4^+}$, cm^{-1}	Γ_{rve}^{+}	$\bar{v}$, cm^{-1}	T, cm^{-1}	$T_{\text{CH}_4^+}$, cm^{-1}
E	103569.8	103601.2	1849.0	E	103574.6	103606.0	1853.8
E	103586.0	103617.4	1865.2	E	103602.0	103633.4	1881.2
E	103620.3	103651.7	1899.5	E	103633.7	103665.1	1912.9
E	103647.1	103678.5	1926.3	E	103655.3	103686.7	1934.5
E	103661.3	103692.7	1940.5	E	103667.7	103699.1	1946.9
E	103704.9	103736.3	1984.1	E	103810.8	103842.2	2090.0
E	103818.1	103849.5	2097.3	E	103835.0	103866.4	2114.2
E	103862.2	103893.6	2141.4	E	103879.8	103911.2	2159.0
E	103897.4	103928.8	2176.6	E	103895.8	103927.2	2175.0
E	103918.6	103950.0	2197.8	E	103922.6	103954.0	2201.8
E	103930.8	103962.2	2210.0	E	103943.5	103974.9	2222.7
E	103960.2	103991.6	2239.4	E	103969.4	104000.8	2248.6
E	103978.8	104010.2	2258.0	E	103991.1	104022.5	2270.3
E	104001.1	104032.5	2280.3	E	104015.7	104047.1	2294.9
E	104056.4	104087.8	2335.6	E	104073.4	104104.8	2352.6
E	104093.7	104125.1	2372.9	E	104125.8	104157.2	2405.0
E	104167.2	104198.6	2446.4	E	104186.8	104218.2	2466.0
E	104194.5	104225.9	2473.7	E	104332.8	104364.2	2612.0
E	104342.7	104374.1	2621.9	E	104350.9	104382.3	2630.1
E	104367.7	104399.1	2646.9	E	104375.6	104407.0	2654.8
E	104516.5	104547.9	2795.7	E	104541.1	104572.5	2820.3
E	104562.1	104593.5	2841.3	E	104573.9	104605.3	2853.1
E	104621.4	104652.8	2900.6	E	104629.1	104660.5	2908.3
E	104650.3	104681.7	2929.5	E	104697.2	104728.6	2976.4
E	104790.0	104821.4	3069.2	E	104876.5	104907.9	3155.7
E	104888.6	104920.0	3167.8	E	104891.8	104923.2	3171.0
F	101741.7	101752.2	0	F	101750.3	101760.8	8.6
F	101752.8	101763.3	11.1	F	101769.9	101780.4	28.2
F	101772.7	101783.2	31.0	F	101775.3	101785.8	33.6
F	101789.6	101800.1	47.9	F	101793.7	101804.2	52.0
F	101803.8	101814.3	62.1	F	101817.7	101828.2	76.0
F	101981.1	101991.6	239.4	F	101985.1	101995.6	243.4
F	101998.2	102008.7	256.5	F	102001.0	102011.5	259.3
F	102004.9	102015.4	263.2	F	102019.5	102030.0	277.8
F	102022.3	102032.8	280.6	F	102033.5	102044.0	291.8
F	102051.0	102061.5	309.3	F	102071.7	102082.2	330.0
F	102089.7	102100.2	348.0	F	102106.9	102117.4	365.2
F	102117.6	102128.1	375.9	F	102124.0	102134.5	382.3
F	102137.2	102147.7	395.5	F	102145.5	102156.0	403.8
F	102150.6	102161.1	408.9	F	102215.2	102225.7	473.5
F	102218.4	102228.9	476.7	F	102237.7	102248.2	496.0
F	102265.7	102276.2	524.0	F	102272.9	102283.4	531.2
F	103440.8	103451.3	1699.1	F	103459.9	103470.4	1718.2
F	103478.3	103488.8	1736.6	F	103553.1	103563.6	1811.4
F	103568.6	103579.1	1826.9	F	103578.4	103588.9	1836.7
F	103588.1	103598.6	1846.4	F	103620.0	103630.5	1878.3
F	103652.0	103662.5	1910.3	F	103657.5	103668.0	1915.8
F	103693.6	103704.1	1951.9	F	103701.5	103712.0	1959.8
F	103712.3	103722.8	1970.6	F	103735.6	103746.1	1993.9
F	103763.2	103773.7	2021.5	F	103790.4	103800.9	2048.7
F	103859.3	103869.8	2117.6	F	103873.8	103884.3	2132.1
F	103908.2	103918.7	2166.5	F	103921.2	103931.7	2179.5
F	103929.1	103939.6	2187.4	F	103954.9	103965.4	2213.2
F	103963.3	103973.8	2221.6	F	103979.0	103989.5	2237.3
F	103983.6	103994.1	2241.9	F	103989.4	103999.9	2247.7
F	103997.4	104007.9	2255.7	F	104028.5	104039.0	2286.8
F	104043.7	104054.2	2302.0	F	104057.2	104067.7	2315.5
F	104069.2	104079.7	2327.5	F	104074.7	104085.2	2333.0
F	104095.2	104105.7	2353.5	F	104104.8	104115.3	2363.1
F	104113.9	104124.4	2372.2	F	104136.6	104147.1	2394.9
F	104149.6	104160.1	2407.9	F	104157.7	104168.2	2416.0
F	104242.8	104253.3	2501.1	F	104247.8	104258.3	2506.1
F	104259.9	104270.4	2518.2	F	104275.2	104285.7	2533.5
F	104293.9	104304.4	2552.2	F	104347.2	104357.7	2605.5
F	104365.1	104375.6	2623.4	F	104503.4	104513.9	2761.7
F	104531.9	104542.4	2790.2	F	104563.6	104574.1	2821.9
F	104578.1	104588.6	2836.4	F	104588.1	104598.6	2846.4
F	104603.6	104614.1	2861.9	F	104631.6	104642.1	2889.9
F	104684.0	104694.5	2942.3	F	105034.7	105045.2	3293.0
F	105043.4	105053.9	3301.7	F	105046.2	105056.7	3304.5
F	105054.3	105064.8	3312.6	F	105075.3	105085.8	3333.6
F	105114.6	105125.1	3372.9	F	105117.3	105127.8	3375.6
F	105124.5	105135.0	3382.8	F	105139.5	105150.0	3397.8
F	105142.4	105152.9	3400.7	F	105145.4	105155.9	3403.7

Table 1 (continued)

Γ_{rve}^{+}	$\bar{v}$, cm^{-1}	T, cm^{-1}	T_{CH4^+}, cm^{-1}	Γ_{rve}^{+}	$\bar{v}$, cm^{-1}	T, cm^{-1}	T_{CH4^+}, cm^{-1}
F	105164.5	105175.0	3422.8	F	105189.1	105199.6	3447.4
F	105194.9	105205.4	3453.2	F	105207.5	105218.0	3465.8
F	105210.3	105220.8	3468.6	F	105223.1	105233.6	3481.4
F	105228.9	105239.4	3487.2	F	105241.7	105252.2	3500.0
F	105317.3	105327.8	3575.6				

spectrum. However, this last explanation seems unlikely because we failed to identify any ground-state combination difference in this spectrum. The intensity differences might help to assign some of the lines from calculations of intensities. Unfortunately, no such calculation has been reported.

Inspection of the term values listed in Table 1 reveals a clustering in two groups of A levels with similar (though not identical) spacings in the regions [255–295 cm^{-1}] and [372–462 cm^{-1}]. This observation might indicate that the main tunneling splitting in this region is already larger than the rotational structure (see Fig. 5 of Ref. [41]). Although the line density in the PFI-ZEKE photoelectron spectrum becomes high already 200 cm^{-1} above the band origin, the spectrum does not become continuous even in the highest wavenumber region studied here, and corresponding to more than 3500 cm^{-1} of internal excitation of CH$_4^+$.

Table 1 lists the positions of 303 rovibronic levels of CH$_4^+$ with internal energy up to 3600 cm^{-1}, 125 of A, 72 of E and 106 of F nuclear-spin symmetry. Given that these levels all have a low value of the rotational quantum number N^+, our data, which are unlikely to include all existing levels, reveal an extremely large density of vibronic (tunneling) levels, only explainable by multidimensional large-amplitude motion, making CH$_4^+$ a fascinating, but also extremely complex molecular system.

The nuclear-spin-symmetry assignments of the origin band have been the key to assign the spectral lines in that band [41]. We expect that they will also help assigning the lines at higher energies when calculations of the rovibronic structure of CH$_4^+$ become available. Progress in this direction has been presented in Section 3, where a two-dimensional model of the large-amplitude motion along the C—H bending modes of e and f$_2$ symmetry is described that predicts vibronic states in the T$_d$ group.

6. Conclusions

The radical cation of methane CH$_4^+$ is an open-shell fluxional molecular system subject to a strong Jahn-Teller effect. Consequently, its energy-level structure and intramolecular dynamics are extremely complex. The rovibrational structures of CH$_4^+$ and its deuterated isotopomers in their electronic ground state have been measured by PFI-ZEKE photoelectron spectroscopy. They are dense and irregular and do not form any recognizable pattern or band structure. Tunneling splittings resulting from the large-amplitude motion of the protons (and deuterons) are of the same order of magnitude as the spacings between adjacent rotational levels. Moreover, the photoelectron spectra do not reveal any ground-state combination differences and cannot be analyzed by the standard methods described in the textbooks of molecular spectroscopy.

This article has summarized studies of the structure and dynamics of CH$_4^+$ by high-resolution photoelectron spectroscopy. Assignments of the rovibronic structures at low energies have gradually emerged from investigations of the effects of isotopic substitution, from IR-VUV double-resonance spectroscopy, and following the development of models of the (ro)vibronic level structure based on the results of *ab initio* quantum-chemical calculations.

The article has also presented new results on CH$_4^+$: First, double-resonance IR-VUV experiments have led to the derivation of the nuclear-spin symmetry and absolute term values of more than 300 levels of CH$_4^+$ with up to about 3500 cm^{-1} of internal excitation. Because all these levels have rotational angular-momentum quantum numbers of at most 3, and considering that it is very unlikely that all such levels have been detected in the energy range investigated experimentally, one must conclude that the density of vibronic levels of CH$_4^+$ is surprisingly high for a five-atomic molecule consisting of light atoms.

Second, a model of the vibronic structure of CH$_4^+$ has been presented that enables the prediction of the vibronic structure arising from the Jahn-Teller effect and the large-amplitude motion resulting from the two (e and f$_2$) C—H bending modes, which are the most active modes in the Jahn-Teller effect of CH$_4^+$. The results of model calculations based on this approach are encouraging: the spacings and density of vibronic levels are in qualitative agreement with those observed experimentally, the vibronic symmetry labels could be derived for the first time in the T$_d$ group, and the potential energy surface along the C-H bending modes reproduces the main features of the surfaces determined *ab initio*.

Despite these successes, the understanding of the structure and dynamics of CH$_4^+$ remains incomplete. Experimentally, the double-resonance experiments described in this article should be extended to the deuterated isotopomers, and more efforts should be invested to measure the intensities of the lines in the PFI-ZEKE photoelectron spectra more precisely than has been possible so far because of the wave-number dependence of the VUV-laser intensity. Theoretically, it would be desirable to develop models of the rovibronic structure that include all vibrational modes and the Jahn-Teller effect, to devise methods to predict the rovibrational line intensities of the photoelectron spectra, and to make predictions of the level structure up to and beyond the T$_d$ structure, where all three diabatic potential curves cross.

References

[1] R. Signorell, Struktur und Dynamik von Molekülkationen, PhD thesis, Eidgenössische Technische Hochschule Zürich, ETH Zurich, Zürich, Switzerland, DISS ETH Nr. 13190, 1999, doi: http://dx.doi.org/10.3929/ethz-a-002094451.
[2] R. Signorell, F. Merkt, The first rotationally resolved spectrum of CH$_4^+$, J. Chem. Phys. 110 (5) (1999) 2309–2311, http://dx.doi.org/10.1063/1.477965.

[3] R. Signorell, F. Merkt, PFI-ZEKE photoelectron spectra of the methane cation and the dynamic Jahn-Teller effect, Faraday Discuss. 115 (2000) 205–228, http://dx.doi.org/10.1039/a909272b.

[4] H.J. Wörner, High-resolution spectroscopic studies of non-Born-Oppenheimer effects, PhD thesis, Eidgenössische Technische Hochschule Zürich, ETH Zurich, Zurich, Switzerland, Diss. ETH Nr. 17081, 2007, doi: http://dx.doi.org/10.3929/ethz-a-005413150.

[5] H.J. Wörner, F. Merkt, Jahn-Teller effects in molecular cations studied by photoelectron spectroscopy and group theory, Angew. Chem. (Int. Ed. Engl.) 48 (35) (2009) 6404–6424, http://dx.doi.org/10.1002/anie.200900526.

[6] E.T. White, J. Tang, T. Oka, CH_5^+: the infrared spectrum observed, Science 284 (5411) (1999) 135–137, http://dx.doi.org/10.1126/science.284.5411.135.

[7] O. Asvany, P. Kumar, B. Redlich, I. Hegemann, S. Schlemmer, D. Marx, Understanding the infrared spectrum of bare CH_5^+, Science 309 (5738) (2005) 1219–1222, http://dx.doi.org/10.1126/science.1113729.

[8] X. Huang, A.B. McCoy, J.M. Bowman, L.M. Johnson, C. Savage, F. Dong, D.J. Nesbitt, Quantum deconstruction of the infrared spectrum of CH_5^+, Science 311 (5757) (2006) 60–63, http://dx.doi.org/10.1126/science.1121166.

[9] C.E. Hinkle, A.S. Petit, A.B. McCoy, Diffusion Monte Carlo studies of low energy ro-vibrational states of CH_5^+ and its deuterated isotopologues, J. Mol. Spec. 268 (1–2) (2011) 189–198, http://dx.doi.org/10.1016/j.jms.2011.04.02.

[10] O. Asvany, K.M.T. Yamada, S. Brünken, A. Potapov, S. Schlemmer, Experimental ground-state combination differences of CH_5^+, Science 347 (6228) (2015) 1346–1349, http://dx.doi.org/10.1126/science.aaa3304.

[11] X.G. Wang, T. Carrington, Calculated rotation-bending energy levels of CH_5^+ and a comparison with experiment, J. Chem. Phys. 144 (20) (2016) 204304, http://dx.doi.org/10.1063/1.4948549.

[12] H. Schmiedt, P. Jensen, S. Schlemmer, Collective molecular superrotation: a model for extremely flexible molecules applied to protonated methane, Phys. Rev. Lett. 117 (2016) 223002, http://dx.doi.org/10.1103/PhysRevLett.117.223002.

[13] J.T. Hougen, Methane Symmetry operations, in: D.A. Ramsay (Ed.), Spectroscopy, International Review of Science, Physical Chemistry, Series Two, vol. 3, Butterworths, London, 1976, pp. 75–125.

[14] G. Herzberg, Molecular spectra and molecular structure, Vol. II: Infrared and Raman Spectra of Polyatomic Molecules, Krieger Publishing Company, Malabar, 1991.

[15] P.R. Bunker, P. Jensen, Molecular Symmetry and Spectroscopy, second ed., NRC Research Press, Ottawa, 1998.

[16] M. Quack, Structure and dynamics of chiral molecules, Angew. Chem. (Int. Ed. Engl.) 28 (5) (1989) 571–586, http://dx.doi.org/10.1002/anie.198905711.

[17] I.B. Bersuker, V.Z. Polinger, Jahn-Teller effect for T terms, Sov. Phys. JETP 39 (1974) 1023.

[18] I.B. Bersuker, The Jahn-Teller Effect, Cambridge University Press, Cambridge UK, 2006.

[19] D. Opalka, W. Domcke, Interpolation of multi-sheeted multi-dimensional potential-energy surfaces via a linear optimization procedure, J. Chem. Phys. 138 (22) (2013) 224103, http://dx.doi.org/10.1063/1.4808358.

[20] U. Öpik, M.H.L. Pryce, Studies of the Jahn–Teller effect. I. A survey of the static problem, Proc. R. Soc. London A 238 (1215) (1957) 425–447, http://dx.doi.org/10.1098/rspa.1957.0010.

[21] J. Arents, L.C. Allen, *Ab Initio* study of the geometries, Jahn-Teller distortions, and electronic charge distribution in the CH_4^+ ion, J. Chem. Phys. 53 (1) (1970) 73–78, http://dx.doi.org/10.1063/1.1673835.

[22] R.N. Dixon, On the Jahn-Teller distortion of CH_4^+, Mol. Phys. 20 (1) (1971) 113–126, http://dx.doi.org/10.1080/00268977100100121.

[23] W. Meyer, PNO-CI Studies of electron correlation effects. I. Configuration expansion by means of nonorthogonal orbitals, and application to the ground state and ionized states of methane, J. Chem. Phys. 58 (3) (1973) 1017–1035, http://dx.doi.org/10.1063/1.1679283.

[24] M.N. Paddon-Row, D.J. Fox, J.A. Pople, K.N. Houk, D.W. Pratt, Dynamic Jahn-Teller effect in methane radical cation. Location of the transition structures for hydrogen scrambling and inversion, J. Am. Chem. Soc. 107 (25) (1985) 7696–7700, http://dx.doi.org/10.1021/ja00311a078.

[25] R.F. Frey, E.R. Davidson, Potential energy surfaces of CH_4^+, J. Chem. Phys. 88 (3) (1988) 1775–1785, http://dx.doi.org/10.1063/1.454101.

[26] K. Takeshita, A theoretical analysis of the Jahn-Teller effect in the photoelectron spectrum of methane, J. Chem. Phys. 86 (1) (1987) 329–338, http://dx.doi.org/10.1063/1.452622.

[27] M.S. Reeves, E.R. Davidson, Potential surface symmetry and vibronic wave functions for methane cation, J. Chem. Phys. 95 (9) (1991) 6551–6561, http://dx.doi.org/10.1063/1.461525.

[28] D. Opalka, W. Domcke, High-order expansion of $t_2 \otimes t_2$ Jahn-Teller potential-energy surfaces in tetrahedral systems, J. Chem. Phys. 132 (15) (2010) 154108, http://dx.doi.org/10.1063/1.3382912.

[29] D. Opalka, W. Domcke, High-order expansion of $t_2 \otimes e$ Jahn-Teller potential-energy surfaces in tetrahedral systems, Chem. Phys. Lett. 494 (4–6) (2010) 134–138, http://dx.doi.org/10.1016/j.cplett.2010.06.

[30] H.J. Wörner, R. van der Veen, F. Merkt, The Jahn-Teller effect in the methane cation: rovibronic structure and the geometric phase, Phys. Rev. Lett. 97 (17) (2006) 173003, http://dx.doi.org/10.1103/PhysRevLett.97.173003.

[31] G. Herzberg, H.C. Longuet-Higgins, Intersection of potential energy surfaces in polyatomic molecules, Discuss. Faraday Soc. 35 (1963) 77–82, http://dx.doi.org/10.1039/DF9633500077.

[32] L.B. Knight Jr., J. Steadman, D. Feller, E.R. Davidson, Experimental evidence for a C_{2v} ($^2B_1$) ground-state structure of the methane cation radical: ESR and ab initio CI investigations of methane cation radicals (CH_4^+ and $CD_2H_2^+$) in neon matrixes at 4 K, J. Am. Chem. Soc. 106 (12) (1984) 3700–3701, http://dx.doi.org/10.1021/ja00324a066.

[33] L.B. Knight Jr., G.M. King, J.T. Petty, M. Matsushita, T. Momose, T. Shida, Electron spin resonance studies of the methane radical cations ($^{12,13}CH_4^+$, $^{12,13}CDH_3^+$, $^{12}CD_2H_2^+$, $^{12}CD_3H^+$, $^{12}CD_4^+$) in solid neon matrices between 2.5 and 11 K: analysis of tunneling, J. Chem. Phys. 103 (9) (1995) 3377–3385, http://dx.doi.org/10.1063/1.470222.

[34] M. Matsushita, T. Momose, T. Shida, L.B. Knight Jr., Group theoretical study of the radical cation of methane: the effect of tunneling motions on the hyperfine interaction, J. Chem. Phys. 103 (9) (1995) 3367–3376, http://dx.doi.org/10.1063/1.470221.

[35] D.S. Gemmell, E.P. Kanter, W.J. Pietsch, Experimental confirmation of the Jahn-Teller distortion of CH_4^+, J. Chem. Phys. 72 (2) (1980) 1402–1404, http://dx.doi.org/10.1063/1.439206.

[36] Z. Vager, Structure of small molecules via the Coulomb explosion method, in: R. Naaman, Z. Vager (Eds.), The Structure of Small Molecules and Ions, Plenum Press, New York, 1988, pp. 105–111.

[37] Z. Vager, T. Graber, E.P. Kanter, D. Zajfman, Direct observation of nuclear rearrangement in molecules, Phys. Rev. Lett. 70 (23) (1993) 3549–3552, http://dx.doi.org/10.1103/PhysRevLett.70.3549.

[38] D. Kella, Z. Vager, A detailed study of conformations in the ground state of CH_4^+, J. Chem. Phys. 102 (21) (1995) 8424–8430, http://dx.doi.org/10.1063/1.468833.

[39] R. Signorell, M. Sommavilla, F. Merkt, Jahn-Teller distortion in $CD_2H_2^+$ from a rotationally resolved photoelectron spectrum, Chem. Phys. Lett. 312 (2-4) (1999) 139–148, http://dx.doi.org/10.1016/S0009-2614(99)00949-5.

[40] R. Signorell, M. Sommavilla, CH_4^+: a fluxional ion?, J Electron. Spectrosc. Relat. Phenom. 108 (1-3) (2000) 169–176, http://dx.doi.org/10.1016/S0368-2048(00)00126-2.

[41] H.J. Wörner, X. Qian, F. Merkt, Jahn-Teller effect in tetrahedral symmetry: large-amplitude tunneling motion and rovibronic structure of CH_4^+ and CD_4^+, J. Chem. Phys. 126 (14) (2007) 144305, http://dx.doi.org/10.1063/1.2712840.

[42] H.J. Wörner, F. Merkt, Jahn-Teller effect in CH_3D^+ and CD_3H^+: conformational isomerism, tunneling-rotation structure, and the location of conical intersections, J. Chem. Phys. 126 (15) (2007) 154304, http://dx.doi.org/10.1063/1.2716394.

[43] M. Grütter, H.J. Wörner, F. Merkt, Rovibronic analysis of the Jahn-Teller effect in $CH_2D_2^+$ at low energies, J. Chem. Phys. 131 (2) (2009) 024309, http://dx.doi.org/10.1063/1.3157210.

[44] M.S. Child, Q. Zhu, Vibration-rotation Hamiltonian of tetrahedral molecules in the local-mode model, Chem. Phys. Lett. 184 (1–3) (1991) 41–44, http://dx.doi.org/10.1016/0009-2614(91)87161-4.

[45] A. Bohm, A. Mostafazadeh, H. Koizumi, Q. Niu, J. Zwanziger, The Geometric Phase in Quantum Systems: Foundations, Mathematical Concepts and Applications in Molecular and Condensed Matter Physics, Springer, Heidelberg, 2003.

[46] C.C. Chancey, M.C.M. O'Brien, The Jahn-Teller Effect in C_{60} and Other Icosahedral Complexes, Princeton University Press, Princeton, 1997.

[47] S. Zilberg, Y. Haas, Electronic degeneracies in symmetric (Jahn-Teller) and nonsymmetric aliphatic radical cations: global topology of σ-bonded molecules, J. Am. Chem. Soc. 125 (7) (2003) 1810–1820, http://dx.doi.org/10.1021/ja028820u.

[48] K. Müller-Dethlefs, E.W. Schlag, High-resolution zero kinetic energy (ZEKE) photoelectron spectroscopy of molecular systems, Ann. Rev. Phys. Chem. 42 (1991) 109–136, http://dx.doi.org/10.1146/annurev.pc.42.100191.000545.

[49] L. Zhu, P. Johnson, Mass analyzed threshold ionization spectroscopy, J. Chem. Phys. 94 (8) (1991) 5769–5771, http://dx.doi.org/10.1063/1.460460.

[50] U. Hollenstein, R. Seiler, H. Schmutz, M. Andrist, F. Merkt, Selective field ionization of high Rydberg states: application to zero-kinetic-energy photoelectron spectroscopy, J. Chem. Phys. 115 (12) (2001) 5461–5469, http://dx.doi.org/10.1063/1.1396856.